COBEM-2023-1796
STUDY OF AXIAL SEPARATORS THROUGH THE COMPUTATIONAL FLUID DYNAMICS TECHNIQUE

Felipe Bendinelli Murça
Fabio de Assis Ressel Pereira
Michel de Oliveira dos Santos
Bruno Loureiro
Federal University of Espírito Santo - Vitória, ES, Brazil.
felipebmurca@gmail.com, fabio.a.pereira@ufes.br, michel.saints@gmail.com, bruno.loureiro@ufes.br

Abstract. *This paper presents a comprehensive computational fluid dynamics (CFD) study of an axial separator, with a focus on investigating the impact of geometries and inlet velocity on key parameters. These parameters include pressure loss, axial and tangential velocities, Euler number and G-force, which directly influence the separator's energy efficiency and separation effectiveness. The study employs a single-phase approach to reduce computational costs while still providing valuable information about the system. Three different geometries were evaluated at four input speeds: 1, 1.5, 2 and 3 m/s. Each geometry has cross-sectional area reductions based on the 75% and 60% decrease in the radial dimension of the swirl generator in comparison to the initial configuration, respectively. The results of the study revealed the formation of recirculation regions and free swirl generation in the core of the separator for high tangential velocity conditions. In general, the study serves as a basis for a better understanding of fluid dynamic phenomena and becomes a precursor for optimization of axial separators.*

Keywords: *CFD, Numerical simulation, Axial Hydrociclone*

1. INTRODUCTION

Multiphase fluid separation is widely utilized in various industrial sectors, including oil extraction, mining, and environmental control systems. Efficient separation of the interesting fluid from other constituents is essential to minimize energy loss and maximize productivity. While numerous technologies have been employed for fluid separation, the hydrocyclone separator has garnered significant attention. The axial separator, a specific hydrocyclone separator, uses inertial and centrifugal forces to separate phases with different densities. These phases can be combinations of liquid-solid, liquid-liquid, or liquid-gas. Enhancing the efficiency of the separation process is crucial to achieving optimal performance and operational effectiveness. In the oil extraction process, for example, gravity separation tanks are commonly employed. However, axial separators offer several advantages in comparison to conventional methods, like enabling in-line separation, requiring less space, having lower costs, and providing faster separation times.

Nieuwstadt and Dirkzwager (1996) was the pioneer of the development of axial separators, initiating studies to understand the fundamental flow characteristics. Subsequently, extensive research combining experimental and numerical approaches has been realized to optimize this new device. Recent technological advancements in computational processing and numerical modeling have propelled the field of fluid dynamics simulation forward. Computational Fluid Dynamics (CFD) allows for exploring a wide range of operating conditions and design variations, reducing the need for costly physical prototypes and extensive experimental testing. The study by ying Shi and yu Xu (2015) evaluates the effectiveness of numerical methods in predicting the swirling flow of the continuous phase in an axial separator using the RSM turbulence model. To validate the study, Laser Doppler Anemometry (LDA) was employed, and the results demonstrated a strong correlation with the experimental data, indicating a reliable performance of the numerical approach. Kou *et al.* (2020) emphasizes the influence of initial operating conditions and geometric parameters on the efficiency of the axial hydrocyclone. Additionally, underflow tube were designed to improve performance by allowing reverse flow to be collected through the new orifice.

In this study, the fluid dynamic behavior of flow in the axial separator is evaluated through numerical simulations. The Reynolds Stress turbulence model was used, allowing the capture of complex details of velocity and stress fields in regions of intense turbulence (Dziubak *et al.*, 2023). The separator geometry is referenced by Slot *et al.* (2012), where was adapted two new geometries for the study. Each geometry contains 75 and 60 percent of the reduction in cross-sectional dimension in relation to standard geometry. Also was evaluated four inlet velocities, as 1, 1.5, 2 and 3 m/s. The analysis of velocity contours and pressure loss enables a better understanding of fluid dynamics to ensure proper system operation. Furthermore, the purpose of this study is to become a precursor for optimizing separation efficiency in future works.

2. NUMERICAL MODEL

2.1 Geometry

The axial separator consists basically of three main components: the external pipe (I), the swirl generator (II), and the collector tube (III). The complete system representation is show in the Fig. 1 for better understanding. However, the simulation domain (dashed line) extends from a short distance of $4D$ upstream of the swirl generator to $17D$ from the system origin, located at the tail of the swirl generator. It should be noted that, since the study aims to predict the fluid behavior using a single-phase approach, the collection tube is not included in the fluid domain.

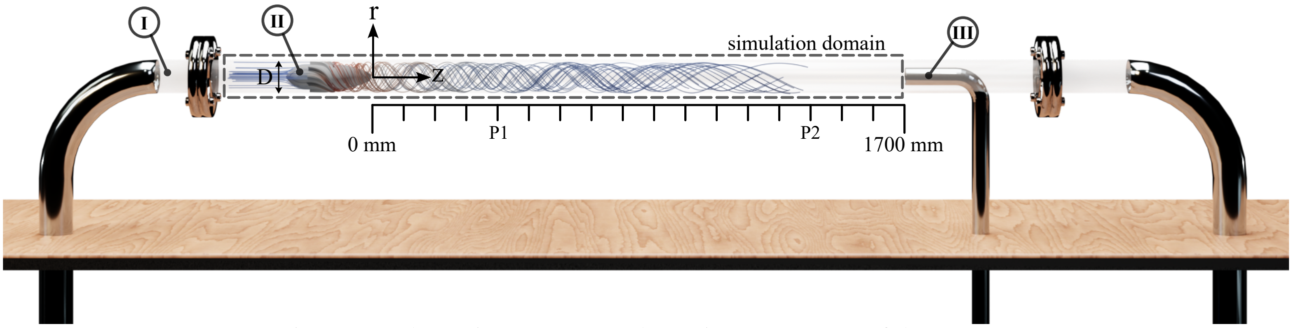

Figure 1: Schematic to represent the main components of the system.

The system dimensions are based on the validation setup by Slot *et al.* (2012). Reference points P1 and P2 are located in 4D and 14D respectively, based on experimental acquisition data for simulation validation. The diameter of the external tube (D) is 100 mm. The fluid flows from the origin of the system to the positive direction of the z-axis. The streamlines represent the generation of swirl as the fluid passes through the swirl generator.

Three different geometries of the swirl generator device were analyzed. The geometries are represented by Geom 100, Geom 75, and Geom 60, as show in Fig. 2. The index indicates the percentage relationship between the radial dimension of the body generator occupied by the new geometry when compared to the reference geometry. Therefore, Geom 75 represents 75% of the radial length of the standard geometry.

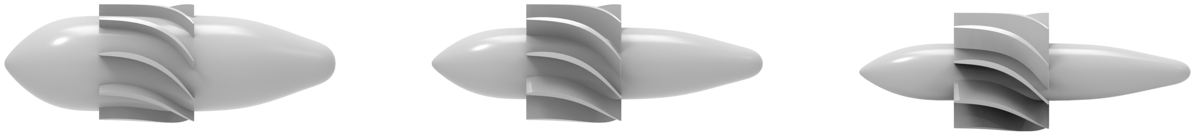

(a) Geom 100 (b) Geom 75 (c) Geom 60

Figure 2: Representation of the swirl generator geometries.

Three distinct flow rates were evaluated in addition to the geometries, corresponding to inlet velocities of 1, 1.5, and 2 m/s. To summarize, a total of 12 unique cases were simulated by combining the created geometries with the aforementioned flow rates.

Another important geometric parameter is the blade profile. For this study, a NACA 4-digit airfoil (NACA, 2023) profile was used, which can be characterized by four main parameters: the maximum curvature (m) as a percentage of the chord (linear distance between the blade's endpoints), the position of the maximum curvature (p), the maximum thickness (t) and the chord length (l). Additionally, the angle of inclination of the blades with respect to the upstream axial direction is 33 degrees. Tab. 1 contains the parameters required to specify the profile of the blades.

Table 1: Parameters of airfoil profile

NACA 4 Digit Airfoil				
Parameter	Max camber (m)	Max camber position (p)	Max thickness (t)	Chord length (l)
Value	17.5 %	50 mm	4.8 mm	100 mm

2.2 Computational mesh

The computational mesh was generated using the commercial software Fluent meshing (2020 R2) using polyhedral elements. Sosnowski *et al.* (2017) studied the influence of mesh types for a cyclone separator and reported many advantages compared to tetrahedral and hexahedral elements, such as the ability to adapt to complex geometries more easily, allowing more accurate representations of irregular surfaces. Additionally, polyhedral elements typically require fewer elements and can also have better quality in terms of distortion. The mesh sensitivity test was conducted to ensure that the numerical results are independent of the mesh discretization level as show in Fig. 4 (b) and (d). The chosen meshes have 4.2, 4.4, and 4.6 million elements for Geom 100, Geom 75, and Geom 60, respectively. The results of the generated mesh for the present study are show in Fig. 3.

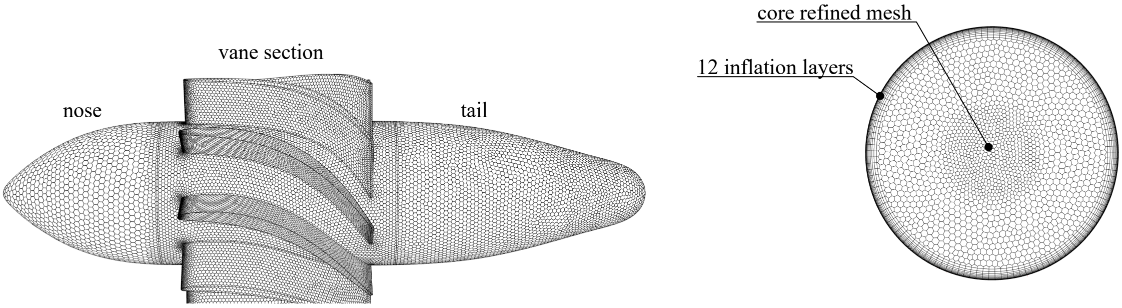

Figure 3: Computational mesh

The swirl generator poses challenges in mesh generation due to its complex regions. Specifically, the area around the trailing edges of the blades present sharp angles between surfaces, necessitating a higher element count for surface conformance. The volume region between the blades also requires meticulous discretization, as it encounters the steepest velocity gradient in the system. Here, fluid flow undergoes directional changes due to blade deflection, resulting in significant centrifugal forces and tangential velocity components. Additionally, the central region of the domain plays a critical role in capturing vortex dissipation, requiring careful refinement, as evident in the cross-sectional view image.

The wall region demands detailed discretization to accurately depict boundary layer development and ensure precise representation of tangential velocities and turbulent flow dissipation. To achieve this, 12 wall layers were added, featuring a growth rate of 40% and an initial element size of 0.065 mm. All generated meshes exhibited an orthogonal quality above 0.5, while maintaining an element aspect ratio below 60, thereby meeting the recommended requirements of the numerical simulation (ANSYS, 2020).

2.3 Numerical methods

The numerical simulations employed the finite volume method with the commercial CFD software ANSYS Fluent (Fluent *et al.*, 2009). Water was chosen as the fluid in this single-phase study, characterized by a density of 1067.8 kg/m³ and a viscosity of 0.001183 kg/m.s (Slot *et al.*, 2012). The simplifying assumptions considered the fluid to be Newtonian, incompressible, and adiabatic. Regarding the boundary conditions, uniform velocity profiles were prescribed at the inlet, no-slip conditions were enforced on the walls, and atmospheric pressure was applied at the outlet.

To describe the strong curvature and rotation of streamlines, the Reynolds stress model (RSM) was employed for its ability to predict anisotropic turbulence and capture vortex flow fluctuations (Hoekstra *et al.*, 1999). Due to the oscillatory nature of the problem, the Unsteady Reynolds-Averaged Navier-Stokes (URANS) turbulence model was used. Ruprecht et al. (2002) observed the attenuation of turbulent fluctuations in the vortex core, with the URANS approach, thereby improving simulation accuracy.

The Semi-Implicit Pressure Linked Equations (SIMPLE) algorithm was used to solve the pressure-velocity coupling. The pressure discretization was performed using the PRESTO algorithm, while a 2nd order upwind scheme was applied to the remaining discretization terms for improved computational accuracy. It is important to note that, in this study, the accuracy of the results was evaluated for simulations using a first-order discretization. However, significant quantitative and qualitative numerical discrepancies were observed with the simpler discretization schemes. Therefore, these schemes should not be used to model flows with the level of complexity encountered in axial separators.

Lastly, the time step increment was uniformly set to 10^{-4} s for all simulations, and a convergence criterion of 10^{-3} was applied to all terms. Despite variations in residence time due to inlet flow rate, all simulations were carried out for a flow time of 2 seconds, ensuring a steady condition for the transient simulation in all evaluated cases. Tab. 2 presents a summary of the setup used for the simulation.

Table 2: Summary table of numerical setups for the simulation.

Parameters		Value
Fluid properties	density	1067.8 kg/s
	viscosity	0.001183 kg/m.s
Global settings	flow state	unsteady
	gravity	9.81 m/s²
Boundary condition	inlet	1, 1.5, 2 and 3 m/s
	outlet	outflow (0 kPa)
	wall	no-slip
Turbulence	model	RSM
	enhancement	curvature correction
	wall function	standard
Solution	pressure-velocity coupling	SIMPLE
	spatial discretization	LSCB
	pressure interpolation	PRESTO!
	momentum	2nd order upwind
	turbulent kinetic energy	2nd order upwind
	dissipation rate	2nd order upwind
	reynolds stresses	2nd order upwind
Calculation	number of iteration	20000
	time step size	0.0001 s

All cases were run on a Dell T7820 Workstation with an Intel® Xeon® Gold 6254 processor (24.75 MB cache, 18 cores, 36 threads, 3.10 GHz to 4.00 GHz Turbo) and 256 GB of GDDR4 RAM. For the simulations, 16 cores were utilized. An average time of 72 hours was required to perform each case. In low-speed conditions, the iterations converged more quickly.

3. GOVERNING EQUATIONS

3.1 Continuity

The continuity is a fundamental equation in fluid mechanics that describes the conservation of mass in a flow. It states that the rate of change of mass within a control volume is equal to the net rate of mass inflow and outflow through its boundaries (Fox *et al.*, 2020). The continuity equation is show in Eq. (1).

$$\frac{\partial \rho}{\partial t} + \frac{\partial (\rho u)}{\partial x} + \frac{\partial (\rho v)}{\partial y} + \frac{\partial (\rho w)}{\partial z} = 0 \tag{1}$$

where ρ represents the fluid density, t is the time, u, v, and w are the velocity components of the fluid in the x, y, and z directions, respectively.

3.2 Momentum

The momentum equation describes the balance between the rates of change of momentum, convective transport of momentum, pressure forces, viscous forces, and gravitational forces in a fluid flow. It provides important insights into the behavior and dynamics of fluid motion. The momentum equation for a three-dimensional and transient flow is given by Eq. (2).

$$\frac{\partial (\rho \mathbf{V})}{\partial t} + \frac{\partial (\rho u \cdot \mathbf{V})}{\partial x} + \frac{\partial (\rho v \cdot \mathbf{V})}{\partial y} + \frac{\partial (\rho w \cdot \mathbf{V})}{\partial z} = -\frac{\partial p}{\partial x} + \mu \left(\frac{\partial^2 \mathbf{V}}{\partial x^2} + \frac{\partial^2 \mathbf{V}}{\partial y^2} + \frac{\partial^2 \mathbf{V}}{\partial z^2} \right) + \rho \mathbf{g} \tag{2}$$

in this equation, ρ represents the density of the fluid, $\mathbf{V}$ is the three-dimensional velocity vector, p is the pressure, μ is the dynamic viscosity of the fluid, and $\mathbf{g}$ is the acceleration vector due to gravity.

3.3 Reynolds stress turbulent model

The RSM (Reynolds Stress Model) is widely recognized for its ability to capture anisotropic turbulence, making it a suitable choice for simulating complex swirling flows. Accordingly, this model was selected for the study. The transport equations of the RSM turbulent model can be defined as show in Eq. (3):

$$\underbrace{\frac{\partial}{\partial t}(\overline{u_i'u_j'})}_{\text{Temporal Term}} + \underbrace{\frac{\partial}{\partial x_k}(\rho u_k \overline{u_i'u_j'})}_{C_{ij}\text{ = Convection}} = \underbrace{-\frac{\partial}{\partial x_k}\left[\rho\overline{u_i'u_j'u_k'} + \overline{p'(\delta_{kj}u_i' + \delta_{ik}u_j')}\right]}_{D_{T,ij}\text{ = Turbulent Diffusion}} + \underbrace{\overline{p'\left(\frac{\partial u_i'}{\partial x_j} + \frac{\partial u_j'}{\partial x_i}\right)}}_{\phi_{ij}\text{ = Pressure Strain}} \quad \cdots$$

$$\underbrace{-\rho\left(\overline{u_i'u_k'}\frac{\partial u_j}{\partial x_k} + \overline{u_j'u_k'}\frac{\partial u_i}{\partial x_k}\right)}_{P_{ij}\text{ = Stress Production}} \underbrace{-2\mu\overline{\frac{\partial u_i'}{\partial x_k}\frac{\partial u_j'}{\partial x_k}}}_{\epsilon_{ij}\text{ = Dissipation}} + \underbrace{S}_{\text{Source Term}} \tag{3}$$

the reynolds stress tensor is represented by $\rho\overline{u_i'u_j'}$. The terms $D_{T,ij}$, P_{ij}, ϕ_{ij}, ϵ_{ij} and C_{ij} refer to turbulent diffusion, stress production, pressure strain, dissipation, and convective term, respectively. It is important to note that in the present study, the source term is set to zero as there is no energy production.

3.4 Euler number

The Euler number is a dimensionless number directly related to energy consumption, expressed as the ratio between the local pressure drop and the kinetic energy of the fluid, defined by Eq. (4) (Babaoğlu *et al.*, 2021).

$$Eu = \frac{\Delta p}{\frac{1}{2}\rho V_{in}^2} \tag{4}$$

where Δp is the pressure drop and V_{in} is the velocity at the inlet.

3.5 G force

The G-force is a dimensionless number used to quantify the centrifugal force. It is defined as the ratio between the centrifugal force and the force of gravity. This force arises from the fluid's inertia in motion and acts radially outward from the center of rotation. It is directly proportional to the angular velocity and distance from the center of rotation (Zeng *et al.*, 2021a). The G-force equation is show in Eq. (5).

$$G = \frac{u_t^2}{r\,g} \tag{5}$$

where u_t is the tangential velocity, r is the radial distance and g is the gravity.

4. RESULTS

4.1 Validation

The experimental validation was conducted using data by (Slot *et al.*, 2012), where the dimensions and geometries of the axial separator were replicated in this study to characterize the numerical model and subsequently adapt the device for different conditions. The boundary conditions for the validation case have inlet velocity of 2 m/s and Geom 100. A notable aspect of the validation case, which differs from the models studied in this report, is the inclusion of a flow rectifier in the physical experiment to prevent reverse flow at the external outlet. However, this component was not incorporated into the numerical model. Tangential and axial velocity data were recorded using Laser Doppler Anemometer (LDA) at positions P1 ($4D$) and P2 ($14D$). The experimental and numerical results are show in Fig. 4. Through validation, it is possible to identify the points that best approximate the experimental velocity profile and understand the areas where the numerical model represents it most accurately, as well as its limitations. Although it is a robust turbulence model, the RSM (Reynolds Stress Model) is based on Reynolds Average Navier Stokes (RANS), which considers averaged values for the velocity and stress components in the flow.

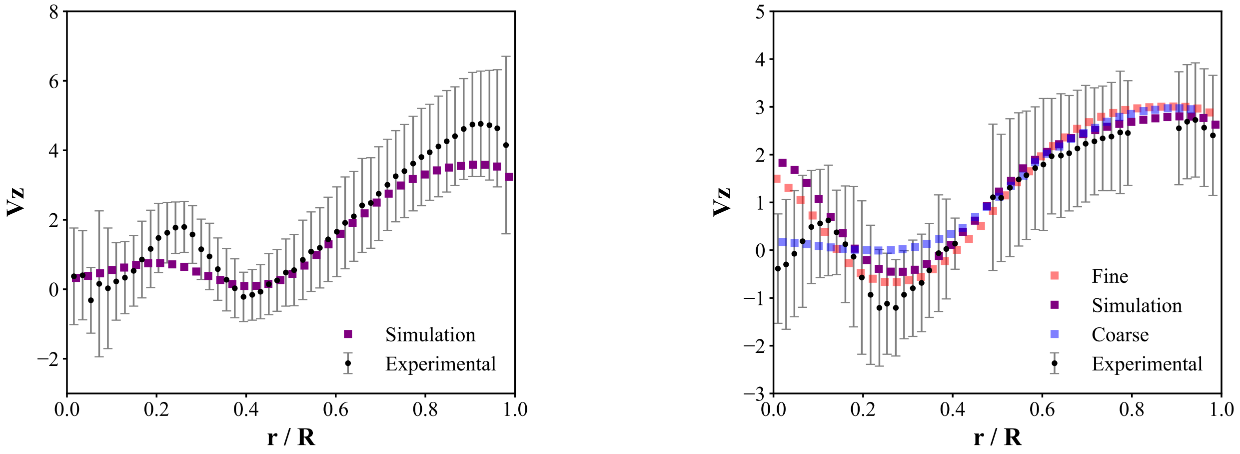

(a) Axial velocity at $4D$ (b) Axial velocity at $14D$

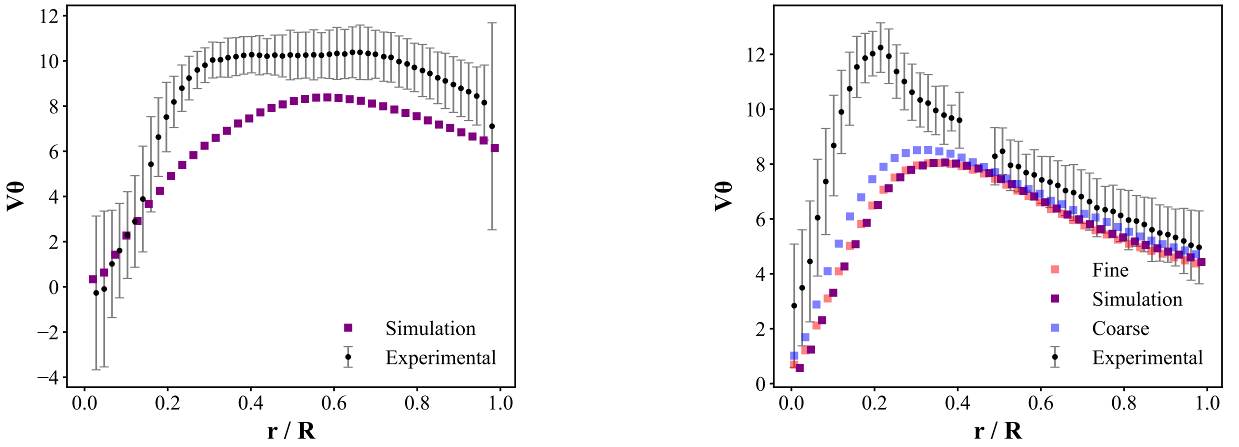

(c) Tangential velocity at $4D$ (d) Tangencial velocity at $14D$

Figure 4: Comparison axial and tangential velocity profile between experimental (LDA) and numerical simulation at $4D$ and $14D$.

Given the oscillatory nature of the physical phenomenon, regions with occasional deviations from the experimental velocity profile can be observed. The numerical model underestimates the tangential components at P1 by approximately 7% for r/R between 0.5 and 1.0, as shown in Fig. 4c. This is reasonable considering that the simulation profile is represented for a specific flow time (2 seconds). Between 0.1 and 0.25 r/R, there is a significant local deviation in the tangential components observed at $14D$. This deviation is due to the complexity of modeling the dissipative terms of the velocity components along the flow, as the reduction in magnitude of the tangential velocity is converted into axial velocity as the flow progresses through the pipe in search of a developed profile. Additionally, another factor contributing to the divergence from the experimental profile is the absence of the collector tube in the numerical model, which creates a pressure differential near the system's outlet and consequently influences the profile in that region. In general, the axial components show a good fit both near the separator geometry and at the outlet.

5. Tangential velocity

Several authors emphasize the important role of tangential velocity in the separation efficiency of a hydrocyclone (Liu *et al.*, 2023). The main driving force in the separation process is the centrifugal force, which is formed from the tangential component of velocity. The fluid enters the separator with a predominantly axial profile, but as it passes through the sharp reduction in cross-sectional area associated with a deviation in flow direction due to the vanes, there is a significant increase in these tangential components of velocity. Consequently, a swirling flow is generated. The tangential velocity profile at $14D$ is show in Fig. 5, where the geometry and inlet velocity influence are evaluated in Fig. 5a and Fig. 5b, respectively.

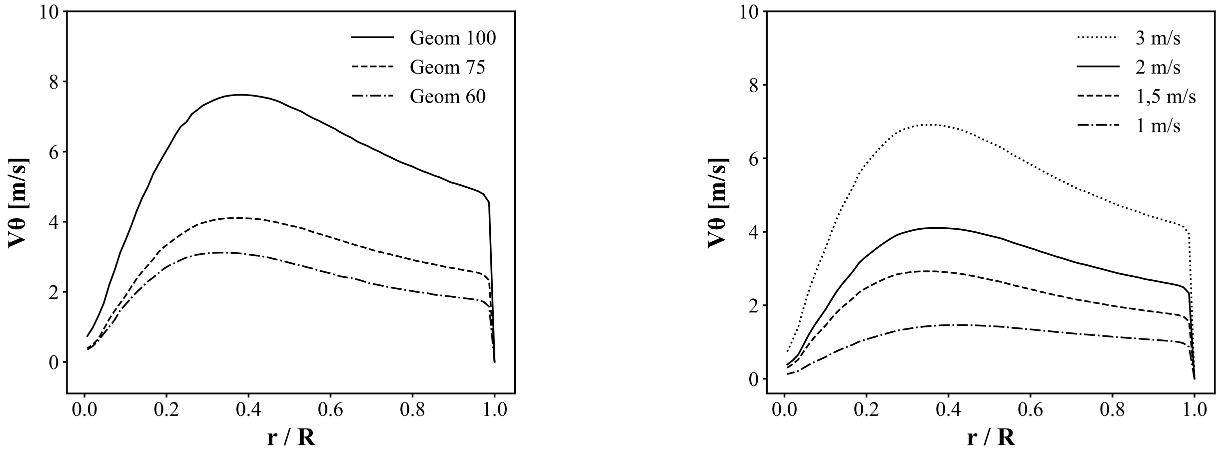

(a) Inlet velocity of 2 m/s

(b) Geom 75

Figure 5: Effect of geometry (a) and inlet velocity (b) in the tangential velocity V_θ at $14D$

.

Mao *et al.* (2023) and Zeng *et al.* (2021a) reported the same behavior for the tangential velocity profiles show in Fig. 5. It can be observed that there is a region with velocities close to zero at the center of the flow due to the low-pressure region located in the core of the separator, caused by the displacement of fluids towards regions near the pipe wall. The graph of Fig. 5a shows the variation of tangential velocity with changes in geometry for an inlet velocity of 2 m/s. The largest difference observed is in the maximum tangential velocity component, which decreased from 7.4 m/s in Geom 100 to 4.1 m/s in Geom 75 and 3.1 m/s in Geom 60. In percentage terms, there were consecutive reductions of 25 and 30%. Note in Fig. 5b the reduced impact of decreasing the inlet velocity on the axial velocity for higher inlet velocities compared to lower inlet velocities. The reduction of 0.5 m/s in the inlet velocity from 2 m/s resulted in a decrease of 30%. Furthermore, when further reducing the inlet velocity to 0.5 m/s (condition of 1 m/s), the maximum tangential velocity is reduced by 48%.

In summary, smaller magnitudes of inlet velocity lead to smaller variations in tangential velocity. Larger reductions in geometry have a less noticeable impact on maximum tangential speed. Furthermore, it is important to note that for all analyzed cases, the maximum velocity region remained similar, indicating a low variation in velocity profile characteristics. The position of the maximum tangential speeds is between 0.25 and 0.4 r/R. Although the position of the point of maximum tangential velocity does not vary significantly with changes in geometry and velocity parameters, it does change along the length of the separator. As the fluid passes through the vortex generator, its maximum tangential component can be found closer to the wall and with greater magnitude. As soon as the fluid flows, wall friction and viscous friction are responsible for dissipating part of this kinetic energy, and the fluid begins to redistribute velocities, shifting the point of maximum velocity towards the central region. For a better understanding of the mentioned phenomena, Fig. 6 presents a longitudinal plane of tangential velocity.

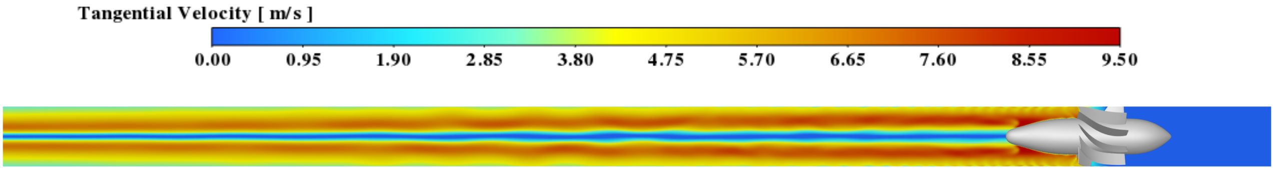

Figure 6: Tangential velocity distribution along the longitudinal plane for Geom 75 with inlet velocity of 3 m/s.

5.1 Axial velocity

Axial velocity is a crucial component in ensuring system performance as it directs the separated fluid fraction towards a collector, as demonstrated in the study conducted by Zeng *et al.* (2021b) on an axial water and oil separator. The separation efficiency is related to the mass flow rate of the secondary phase leaving the collector (m_{out}) in relation to the fraction of the secondary phase at the system inlet (m_{in}), with efficiency (η) represented by $\eta = 1 - (m_{out}/m_{in})$. It is important to note that the intensity of the outlet fraction is directly related to the axial flow rate of the system, given by $m_{out} = \rho\ V_z\ A$, where Vz is the axial velocity. Understanding its relevance, axial velocity is analyzed in Fig. 7, considering variations in geometry and velocity along the length of the separator.

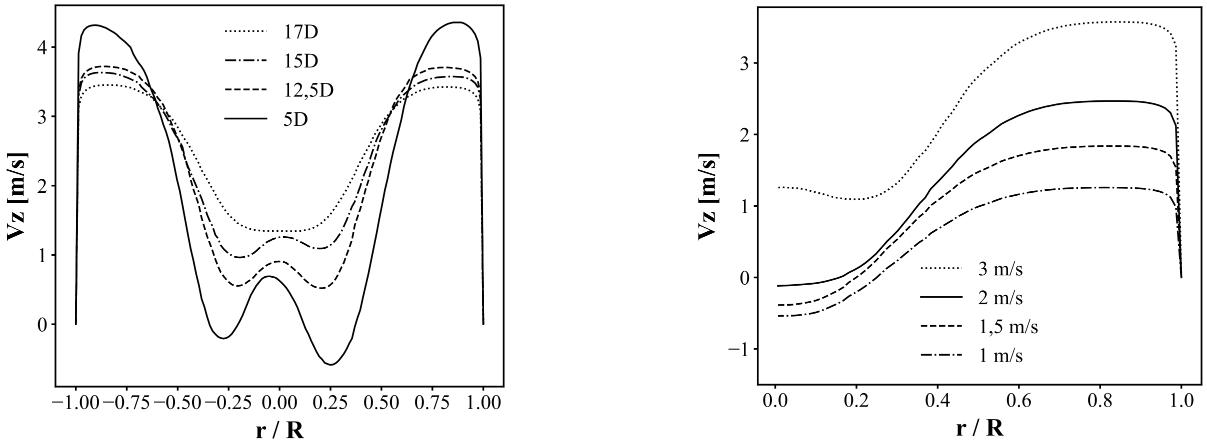

(a) Inlet velocity of 2 m/s, Geom 75.

(b) Geom 75

Figure 7: Evaluation of the effect of geometry (a) and inlet velocity (b) on the axial velocity profile V_z.

To ensure high separation efficiency, an axial hydrocyclone separator must not only promote phase separation but also maintain an appropriate axial velocity. As the fluid flows along the pipeline, the tangential components dissipate until the profile becomes fully developed. However, high tangential velocities cause the formation of an internal vortex, known as a free vortex, intensifying the axial components at the outlet. Fig. 7b shows the axial velocity profile at $14D$ for Geom 75 under different inlet velocity conditions. Notably, an increase in the axial velocity component in the central region can be observed starting from 2 m/s. For Geom 60, the free vortex does not form under any inlet conditions, while for Geom 100, the free vortex is formed in all cases due to the large reduction in vane cross-section, as show in Fig. 8.

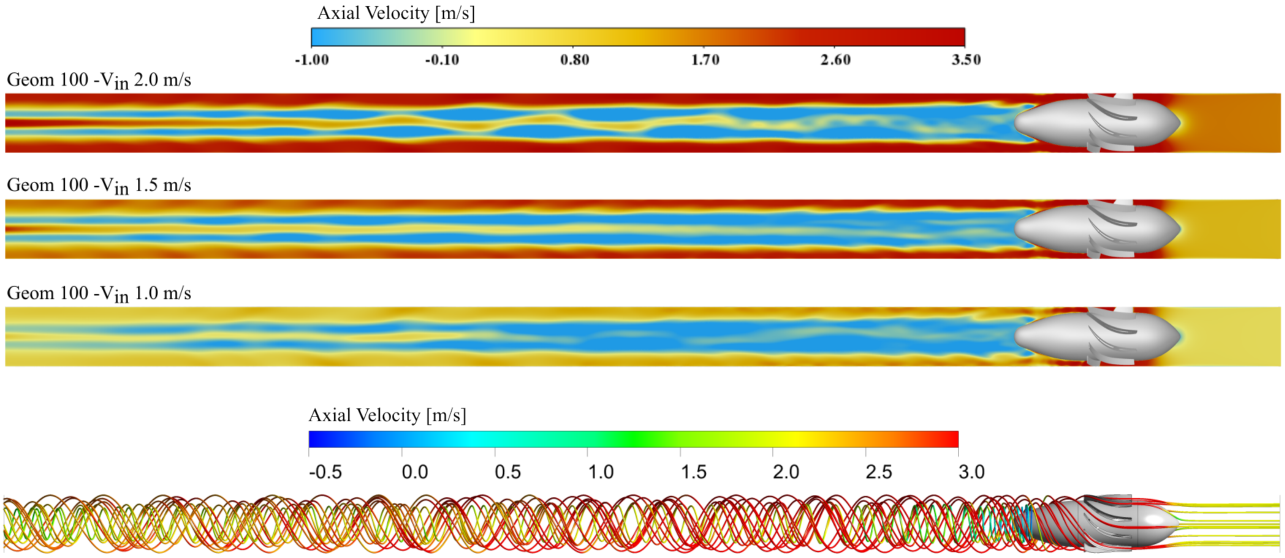

Figure 8: Axial velocity contours for inlet velocities of 1, 1.5 and 2 m/s (Geom 100), and streamline for Vin 2 m/s.

The region formed by the free vortex is surrounded by reverse flow zones, characterized by negative velocities, that create a recirculation region along the core of the separator. Higher entry velocities result in greater magnitudes of the axial component. However, instability in the central flow is observed at intermediate positions of the device. Conditions of 1 and 1.5 m/s provide a more stable flow, although with an increase in the recirculation zone. While the formation of the free vortex is not essential for the separator's functioning, it enhances its performance and efficiency. Additionally, the axial separator can be used with fluids in various physical states, such as liquid-gas and liquid-solid, each requiring evaluation based on its specific characteristics.

6. Pressure loss, Euler number and G force

The pressure drop across the axial separator is evaluated by measuring the static pressure difference between the outlet and the inlet of the system. Several factors influence the pressure drop, including the geometry of the vortex generator device, the fluid inlet velocity, and the energy dissipation due to viscous friction with the walls. To analyze its relationship with the inlet velocity, the Euler number is used. This dimensionless number quantifies the pressure drop relative to the fluid's kinetic energy based on the inlet velocity. Another important parameter analyzed is the G-force, which measures the acceleration experienced by the fluid due to the action of tangential velocity components. As kinetic dissipation occurs along the pipeline, this parameter was measured by averaging over transverse planes along the length (z-axis). Figure 9 presents the pressure drop, Euler number (a), and G-force (b) for all geometries and inlet conditions.

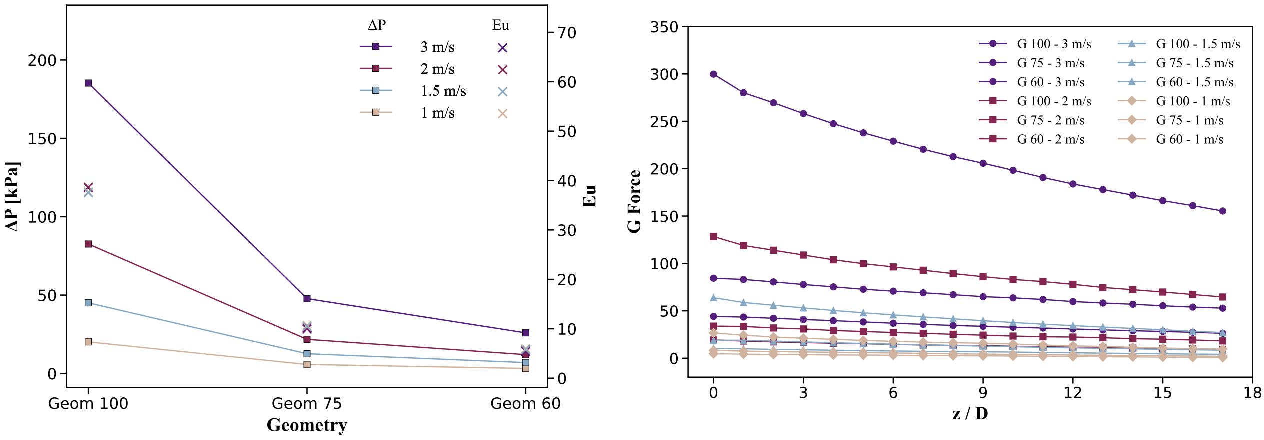

(a) Pressure loss and Euler number

(b) G force

Figure 9: Evaluation of the effect of inlet velocity and swirl generator geometry on Pressure loss, Euler number (a) and G-force (b).

The graph shown in Figure 9 demonstrates that larger geometries are associated with a higher pressure drop, highlighting the significant role of the separator geometry in flow resistance. Similarly, higher inlet velocities result in a greater pressure drop, indicating that increasing the fluid velocity increases resistance and leads to a more pronounced pressure drop. It is worth noting that there is a substantial reduction in pressure drop between Geom 100 and Geom 75, evidencing the direct impact of geometry modification on separator performance. Additionally, for constant velocities, there are consecutive reductions of 73% and 45% in pressure drop between Geom 100, Geom 75, and Geom 60. Similarly, with constant geometries, reductions of 55% are observed between velocities of 3 m/s and 2 m/s, and reductions of 75% from 2 m/s to 1 m/s. The influence of geometric variations on the Euler number is more significant than that of the inlet velocity. About the Euler number, it was possible to observe little variation with changes in geometry. This dimensionless number relates the pressure difference to the kinetic energy of the fluid, which, in turn, exhibits a quadratic term of the velocity. Therefore, the increase in the pressure differential due to a larger obstruction of the geometry increased in the same proportion as the quadratic term of the inlet velocity, resulting in independence from this parameter. Regarding the G-force shown in Fig. 9b, good agreement with values from other studies has been observed (Zeng *et al.*, 2021a). However, the case with an inlet velocity of 3 m/s for Geom 100 exhibited notably higher centrifugal forces compared to the other cases. This can be attributed to a significant increase in maximum tangential velocities in the blade section, as the G-force equation squares the term for tangential velocity. The graph in Fig. 10 illustrates the pressure distribution in the axial separator for the case of Geom 75 with an inlet velocity of 3 m/s. It can be observed that the pressure decreases from the inlet to the outlet as the fluid flows. In the radial direction, the pressure drop occurs from the tube wall towards the central region. A notable characteristic of turbulent flow is the adverse pressure gradient generated in the core flow due to the fluid displacement towards the wall region. The same qualitative behavior is observed for the other cases evaluated in this study.

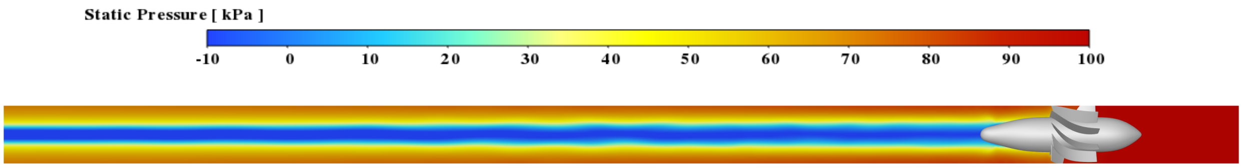

Figure 10: Static pressure distribution along the longitudinal plane for Geom 75 with inlet velocity of 3 m/s.

7. CONCLUSION

This study investigated the fluid dynamic behavior of an axial separator using computational fluid dynamics (CFD) techniques with a Reynolds stress model (RSM). Experimental data from Slot et al. were used to validate the study, with their geometry serving as a reference. Additionally, two new geometries were generated, modifying the radial dimension to evaluate its effects. The studies were conducted for four entry velocity conditions: 1 m/s, 1.5 m/s, 2 m/s and 3 m/s. Key parameters including Euler number, G-force, pressure loss and velocity components were analyzed.

The results revealed the presence of recirculation regions in the core of the separator, extending along the geometry. Under conditions of high tangential velocity, the formation of free vortices was observed, leading to central axial components at the exit of the separator. Geometries with smaller bodies exhibited narrow and elongated recirculation regions, along with lower pressure losses. On the other hand, larger geometries resulted in higher tangential velocities, facilitating free vortex formation, but causing a greater pressure drop. A higher pressure drop indicates lower energy efficiency as it requires a larger pumping system to deliver sufficient energy to the fluid. However, a low pressure gradient can impair the device's separation ability. A significant reduction in pressure drop was observed for the Geom 75, in addition to the stability of the free vortex region.

Overall, this study improves our understanding of fluid dynamics in axial separators and demonstrates the predictive capabilities of turbulent flow behavior. In addition, it highlights the versatility of this tool in understanding fluids in complex flow situations. Furthermore, this study lays the groundwork for future multiphase simulations of axial separators, with a focus on design optimization.

8. REFERENCES

ANSYS, 2020. *Fluent Theory Guide*. ANSYS Inc., Canonsburg, PA.

Babaoğlu, N.U., Parvaz, F., Hosseini, S.H., Elsayed, K. and Ahmadi, G., 2021. "Influence of the inlet cross-sectional shape on the performance of a multi-inlet gas cyclone". *Powder Technology*, Vol. 384, pp. 82–99.

Dziubak, T., Dziubak, S. and Tomaszewski, M., 2023. "Numerical study of the effect of axial cyclone inlet velocity and geometrical parameters on separation efficiency and pressure drop". *Powder Technology*, Vol. 427, p. 118692.

Fluent, A. *et al.*, 2009. "Ansys fluent 12.0 user's guide". *Ansys Inc*, Vol. 15317, pp. 1–2498.

Fox, R.W., McDonald, A.T. and Mitchell, J.W., 2020. *Fox and McDonald's introduction to fluid mechanics*. John Wiley & Sons.

Hoekstra, A., Derksen, J. and Van Den Akker, H., 1999. "An experimental and numerical study of turbulent swirling flow in gas cyclones". *Chemical Engineering Science*, Vol. 54, No. 13, pp. 2055–2065.

Kou, J., Chen, Y. and Wu, J., 2020. "Numerical study and optimization of liquid-liquid flow in cyclone pipe". *Chemical Engineering and Processing - Process Intensification*, Vol. 147, p. 107725.

Liu, M., Kong, C., Zhang, Y., Chen, J. and Peng, S., 2023. "Effect of gas on separation performance of an axial hydrocyclone for preliminary water separation". *Powder Technology*, Vol. 425, p. 118581.

Mao, R., Li, Y., Liu, Y., Zhu, H., Wang, N., Yang, Q. and Lu, H., 2023. "Separation characters of an axial-flow hydrocyclone with oil collecting pipe". *Separation and Purification Technology*, Vol. 305, p. 122139.

NACA, 2023. "NASA: Naca airfoils". `https://www.nasa.gov/image-feature/langley/100/naca-airfoils`. Accessed 21 Jan 2023.

Nieuwstadt, F.T.M. and Dirkzwager, M., 1996. "A fluid mechanics model for an axial cyclone separator". *Industrial & Engineering Chemistry Research*, Vol. 34, pp. 3399–3404.

Slot, Robert Frank, van Campen, L., Mudde, J. and Hoeijmakers, H., 2012. "A numerical and experimental survey of a liquid-liquid axial cyclone". *International journal of chemical reactor engineering*, Vol. 10.

Sosnowski, M., Krzywanski, J. and Gnatowska, R., 2017. "Polyhedral meshing as an innovative approach to computational domain discretization of a cyclone in a fluidized bed clc unit". *E3S Web of Conferences*, Vol. 14, p. 01027.

ying Shi, S. and yu Xu, J., 2015. "Flow field of continuous phase in a vane-type pipe oil–water separator". *Experimental Thermal and Fluid Science*, Vol. 60, pp. 208–212.

Zeng, X., Xu, Y., Zhao, L., Fan, G. and Yan, C., 2021a. "Numerical investigation on axial liquid-liquid separators with different swirl chambers". *Chemical Engineering and Processing - Process Intensification*, Vol. 161, p. 108324.

Zeng, X., Zhao, L., Fan, G. and Yan, C., 2021b. "Numerical and experimental study on a new axial separator for liquid-liquid separation". *Journal of the Taiwan Institute of Chemical Engineers*, Vol. 123, pp. 104–114.

9. RESPONSIBILITY NOTICE

The authors are solely responsible for the printed material included in this paper.